Van der Waals Engineering of Ultrafast Carrier Dynamics in Magnetic Heterostructures

Paulina Ewa Majchrzak, Yuntian Liu, Klara Volckaert, Deepnarayan Biswas, Chakradhar Sahoo, Denny Puntel, Wibke Bronsch, Manuel Tuniz, Federico Cilento, Xing-Chen Pan, Qihang Liu, Yong P. Chen, and Søren Ulstrup*

ABSTRACT: Heterostructures composed of the intrinsic magnetic topological insulator $MnBi_2Te_4$ and its nonmagnetic counterpart Bi_2Te_3 host distinct surface electronic band structures depending on the stacking order and exposed termination. Here, we probe the ultrafast dynamical response of $MnBi_2Te_4$ and $MnBi_4Te_7$ following near-infrared optical excitation using time- and angle-resolved photoemission spectroscopy and disentangle surface from bulk dynamics based on density functional theory slab calculations of the surface-projected electronic structure. We gain access to the out-of-equilibrium charge carrier populations of both $MnBi_2Te_4$ and Bi_2Te_3 surface terminations of $MnBi_4Te_7$, revealing an instantaneous occupation of states associated with the Bi_2Te_3 surface layer followed by carrier extraction into the adjacent $MnBi_2Te_4$ layers with a laser fluence-tunable delay of up to 350 fs. The ensuing thermal relaxation processes are driven by phonon scattering with significantly slower relaxation times in the magnetic $MnBi_2Te_4$ septuple layers. The observed competition between interlayer charge transfer and intralayer phonon scattering demonstrates a method to control ultrafast charge transfer processes in $MnBi_2Te_4$-based van der Waals compounds.

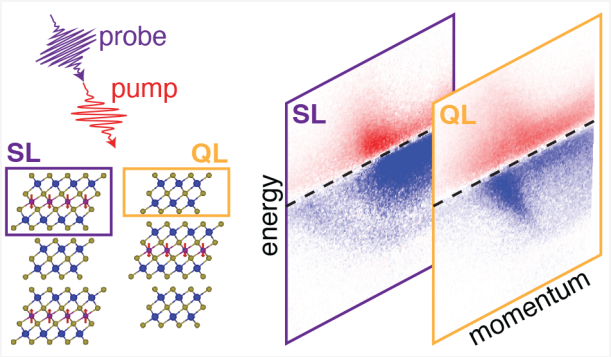

KEYWORDS: *magnetic topological insulators, $MnBi_2Te_4$, van der Waals heterostructures, ultrafast carrier dynamics, time- and angle-resolved photoemission spectroscopy, density functional theory*

Heterojunctions composed of two-dimensional (2D) semiconducting materials are highly promising for developing novel optoelectronic devices due to tunable band gaps and charge carrier dynamics.[1] The interplay of charge and phonon interactions has been intensively examined in transition metal dichalcogenide heterostructures, unveiling a sub-50 fs interlayer carrier extraction that is ideal for light harvesting and photovoltaics.[2,3] van der Waals compounds based on the antiferromagnetic topological insulator $MnBi_2Te_4$ present another attractive candidate for advanced opto- and spintronics applications due to the realization of exotic phases such as the quantum anomalous Hall effect and axion electrodynamics.[4−12] Yet, optically induced ultrafast carrier dynamics and charge transfer processes in these materials remain largely unexplored. Moreover, the properties of these materials can be elegantly engineered via van der Waals stacking. For example, combining a quintuple layer (QL) of the nonmagnetic topological insulator Bi_2Te_3 with a septuple layer (SL) of $MnBi_2Te_4$ reduces the antiferromagnetic exchange interaction between neighboring planes of Mn atoms, while strengthening the affinity of the system to undergo a spin-flop transition to ferromagnetic order.[13] As a result, van der Waals heterostructures of the form $MnBi_2Te_4(Bi_2Te_3)_m$ (m = 1, 2, 3, ...) offer a platform for exploring the interplay between the magnetic properties and the topological phases of matter.[14−21] In order to gain access to the energy- and momentum-resolved ultrafast carrier dynamics of $MnBi_2Te_4(Bi_2Te_3)_m$ heterostructures, we employed time- and angle-resolved photoemission spectroscopy (TR-ARPES). This approach utilizes a near-infrared optical excitation to induce direct optical transitions from the occupied to the unoccupied states. The out-of-equilibrium charge carrier populations in the excited states are then measured by a time-delayed ultraviolet probe pulse, giving direct insights into charge transfer processes and phonon relaxation between bulk and surface states on a given

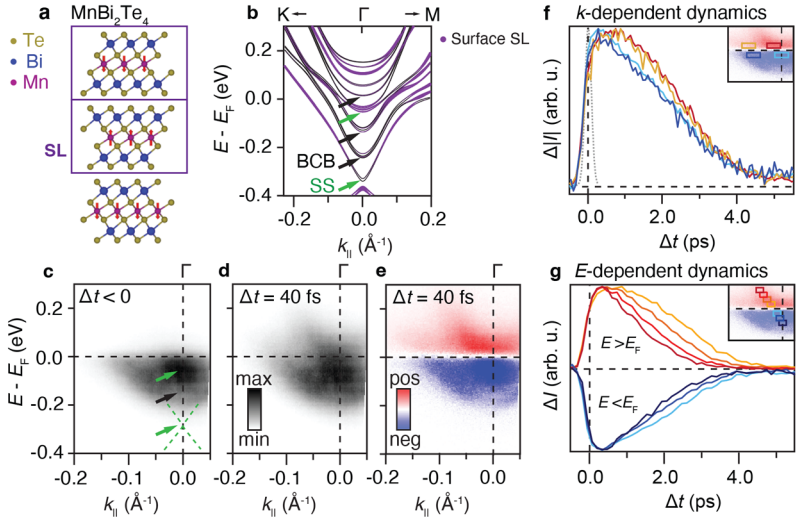

Figure 1. Surface electronic structure and excited state populations in $MnBi_2Te_4$. (a) Overview of septuple layer (SL) crystal structure with spins on Mn atoms indicated by red arrows. (b) DFT slab calculation of surface-projected band structure shown as black curves with the weight of the projected bands indicated by purple circles. (c–e) Photoemission intensity (c) before the arrival of the pump pulse ($\Delta t < 0$) and (d) in the initial stage of excitation (Δt = 40 fs) with a laser fluence of 280 μJ/cm^2. (e) Intensity difference spectrum obtained by subtracting the equilibrium spectrum in (c) from the excited state signal in (d). The spectra were collected around the Γ-point of the Brillouin zone. The green and black arrows in parts (b) and (c) indicate the surface and bulk bands, respectively. The dashed green lines in (c) indicate the expected dispersion of the topological surface state. (f) Absolute value of normalized intensity difference integrated within the (E, k)-regions demarcated by correspondingly colored boxes in the inset as a function of time delay. (g) Normalized intensity difference integrated within (E, k)-regions demarcated by the colored boxes centered at varying energies placed along the most intense excited band, as shown in the inset. The intensity differences in the insets in parts (f) and (g) are the same as shown in (e).

heterostructure termination.[22] This approach has revealed thermal dynamics with a duration of 4 ps in $MnBi_2Te_4$ across the magnetic ordering temperature[23] as well as photoinduced filling of the surface state hybridization gap of the QL termination in a heterostructure with stoichiometry m = 3.[24] Here, we determine how carrier extraction and relaxation is controlled by the balance of inter- and intralayer interactions by comparing the time-dependent evolution of excited electronic states between the m = 0 and the m = 1 heterostructures, i.e., $MnBi_2Te_4$ and $MnBi_4Te_7$. We observe an excited state population in the QL of $MnBi_4Te_7$ that is generated via an infrared pump pulse. This population is then gradually extracted into the SL with a fluence-dependent delay of up to 350 fs. Thermal relaxation then proceeds at a slower rate within the magnetic SL, implying that the layer-dependent electronic and magnetic properties can be optically controlled on an ultrafast time scale.

Figure 1a presents the SL $MnBi_2Te_4$ structure, which can be thought of as a QL with an intercalated Mn–Te bilayer, introducing a plane of unpaired spins. Nontrivial topology in this system derives from its Te 5p valence band (VB) and Bi 6p conduction band (CB) which undergo band inversion due to spin–orbit coupling (SOC).[25] The corresponding surface-projected electronic structure obtained from density functional theory (DFT) slab calculations is presented in Figure 1b. The surface and bulk states are indicated by green and black arrows, respectively. In the energy range of our measurement, three branches of bulk bands and two surface bands are observed with the order from lower to higher energy of surface–bulk–bulk–surface–bulk around the Γ-point of the Brillouin zone. The two branches of bulk bands with lower energy exhibit weak out-of-plane-dispersion.[26,27]

Figure 1c,d presents the electronic dispersion of $MnBi_2Te_4$ around the Γ-point of the Brillouin zone, measured in equilibrium conditions before optical excitation ($\Delta t < 0$) and during the initial moments of excitation (Δt = 40 fs). Figure 1e shows the photoemission intensity difference resulting from subtraction of the equilibrium spectrum from the excited spectrum. The red (blue) regions correspond to gain (loss) of photoemission signal and can be interpreted as excited electron (hole) populations. The spectra display a broad, nearly parabolic distribution of intensity with a minimum at $E - E_F$ = −0.20 eV, indicating that the as-grown crystals are significantly electron-doped.[28] Note the asymmetric presentation of the $k_\parallel$-scale is due to the fact that we have centered the excited state signal on the detector window, and not the Γ-point, in order to fully capture the dynamics along the band above the Fermi energy E_F. A region of high intensity is concentrated at Γ around $E - E_F$ = −0.05 eV, which is consistent with the location of surface states marked by green arrows in Figure 1b. The fainter background intensity, marked by a black arrow in Figure 1c, is primarily composed of bulk conduction band (BCB) states, as seen via a comparison with Figure 1b. During excitation, we observe that the bands crossing E_F become occupied up to $E - E_F$ = 0.20 eV with high excited state signal above the central surface states. These features have previously been attributed to a Rashba-like spin splitting,[26] suggesting a significant nonequilibrium occupation of spin-polarized carriers in this system. The topological surface state in the bulk band gap (below $E - E_F$ = −0.20 eV), reported to be a gapless Dirac cone in previous works,[29−31] is not resolved due to the low cross-section compared with the CB states at our probe polarization and photon energy.[27]

The time dependence of electron (hole) dynamics in the BCB and surface states is examined by integrating the intensity within an (E, k)-region spanning 40 meV and 0.03 Å^{-1}, respectively, centered ±40 meV above (below) E_F. These integration regions are placed at different k-values for electrons

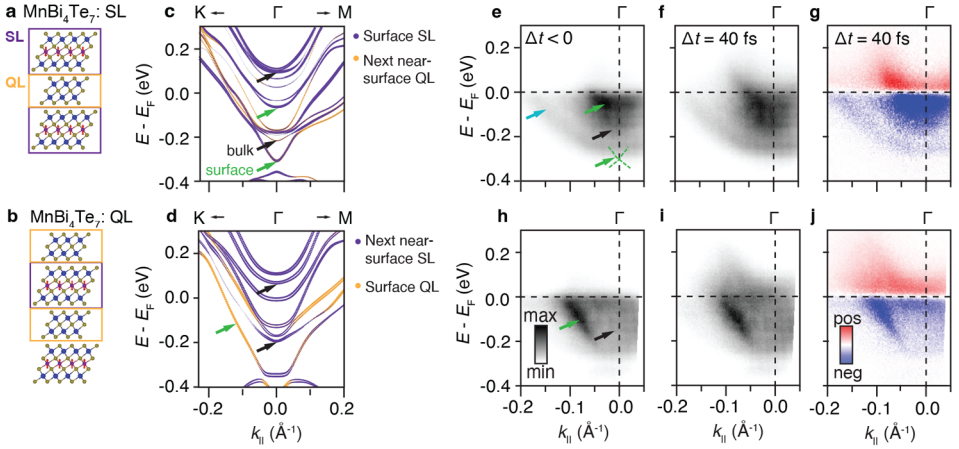

Figure 2. Surface termination dependent electron dynamics in $MnBi_4Te_7$. (a, b) Layered crystal structures of $MnBi_4Te_7$ with a SL or QL exposed at the surface. The red arrows indicate spins on the Mn atoms. (c, d) Dispersions obtained from DFT slab calculations for $MnBi_4Te_7$ with (c) SL and (d) QL termination. The SL projected bands are colored purple, while the QL projected bands are colored orange. (e–j) TR-ARPES spectra and intensity difference for (e–g) SL termination and (h–j) QL termination. The data are presented similarly as for $MnBi_2Te_4$ in Figure 1c–e. The measurements were performed with a laser fluence of 280 $\mu J/cm^2$. Arrows in (c)–(e) and (h) indicate surface (green), bulk (black), and surface-induced Rashba (light blue) bands. Dashed green lines in (e) indicate the expected dispersion of the topological surface state.

and holes in order to track the intensity difference for regions composed mainly of BCB (intensity away from Γ) or surface bands (intensity around Γ). Figure 1f presents the resulting time-dependent intensity around E_F for electrons, represented by red and orange curves, as well as holes, represented by light and dark blue curves that are color-coded according to the integration regions in the inset. The intensity due to excited carriers initially matches the pump–probe cross-correlation integral (see the dashed peak in Figure 1f). The increase in signal then slows down before reaching a plateau, which is followed by a decay back to equilibrium that is achieved around 5 ps after the excitation. The intensity difference corresponding to excited holes at −40 meV reaches its maximum at $\Delta t \approx 0.2$ ps. For excited electrons at 40 meV, the maximum excitation density is achieved significantly later at $\Delta t \approx 0.8$ ps. The E-dependent decay dynamics is determined by inspecting the intensity difference integrated in (E, k)-regions tracking the intense surface band, as shown in Figure 1g. The signal furthest from E_F rapidly increases during excitation and then decays exponentially, while the transient population of excited electrons closer to E_F builds up more slowly. This behavior is consistent with the cascading of intraband scattering processes from higher-lying states.[32,33] The faster transient buildup of holes close to E_F observed in Figure 1f,g reveals an apparent asymmetry in electron and hole dynamics, which is indicative of a shift of the chemical potential induced by the photodoping.[34] Such a shift is demonstrated in Figure S1. The slower decay dynamics of excited electrons and holes close to E_F is driven by the evolution of the electronic temperature and associated Fermi–Dirac distribution after excitation when a quasi-thermal equilibrium is attained.[34]

We now turn to the $MnBi_4Te_7$ heterostructure composed of alternating SL and QL units, as sketched in Figure 2a,b. Cleaving the bulk crystal can expose either of these terminations, which exhibit distinct surface electronic structures that we can separately resolve in our TR-ARPES experiment, as shown in Figure S2. Bulk- and surface-derived bands are distinguished via DFT slab calculations of the surface-projected band structures associated with the two terminations, as shown in Figure 2c,d. The calculated dispersions exhibit a gapped Dirac cone for the SL surface and hybridization bands between the two layers near the QL surface, in agreement with previous studies.[19] TR-ARPES spectra acquired within the same energy range for both terminations are presented in Figure 2e–j. Both terminations exhibit a similar level of electron-doping as $MnBi_2Te_4$, causing the photoemission intensity to mainly consist of contributions from BCB and surface states around E_F. Regions of high intensity measured at the SL termination do not coincide with regions of high intensity at the QL termination due to the surface-specific character of these bands (see green arrows in Figure 2e,h). This assignment of band character is supported by the calculations for the SL termination that show bulk bands concentrated in the range of 0.1–0.2 eV below E_F around Γ, whereas the bands immediately below E_F are surface states. Regions of high intensity for the QL termination originate from hybridized surface bands. For both SL and QL terminations, the fainter background signals are consistent with BCB states that are identified via black arrows in Figure 2c–e,h. Finally, the SL termination supports a surface-induced Rashba band marked by a light-blue arrow in Figure 2e, which is not reproduced by DFT calculations.[35,36]

The spectra acquired for $\Delta t = 40$ fs and the intensity difference calculated by subtracting the corresponding spectra measured for $\Delta t < 0$ in Figure 2f,g,i,j reveal significant electron and hole populations in the surface band around Γ at the SL termination, whereas the QL termination exhibits a strong signal due to holes in the surface band and mainly excited electrons in the bulk states above E_F upon photoexcitation. The time-dependence of the intensity difference in selected (E, k)-regions is analyzed for the two terminations in Figure S3, similarly as shown for $MnBi_2Te_4$ in Figures 1f,g. The asymmetry between excited electron and hole signals driven by a chemical potential shift diminishes from $MnBi_2Te_4$ to SL-terminated $MnBi_4Te_7$ and is absent in QL-terminated $MnBi_4Te_7$, consistent with significant interlayer charge transfer in $MnBi_4Te_7$.

Having established the dispersion and response to photoexcitation across $MnBi_2Te_4$ and both $MnBi_4Te_7$ surface terminations, we are now in a position to disentangle the

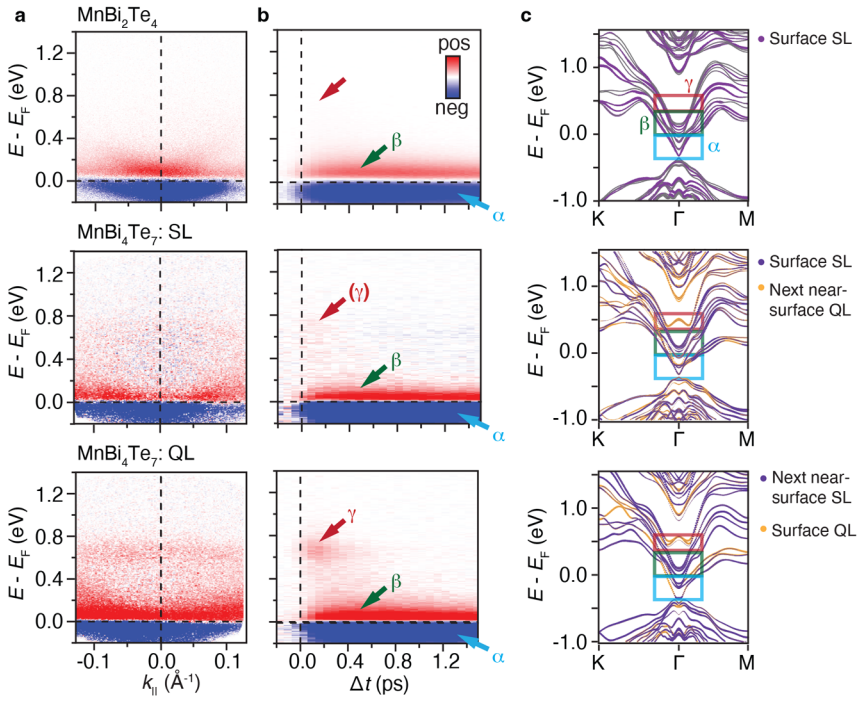

Figure 3. Intra- and interband dynamics in the van der Waals heterostructures $MnBi_2Te_4$ and $MnBi_4Te_7$. (a) Intensity difference spectra of $MnBi_2Te_4$ and SL and QL terminations of $MnBi_4Te_7$ obtained by subtracting an average of the equilibrium spectrum measured at $\Delta t < 0$ from the excited state signal at $\Delta t = 40$ fs. (b) Energy-distribution curves (EDCs) extracted at Γ as a function of time delay for $MnBi_2Te_4$ (top), SL (middle), and QL (bottom) terminations of $MnBi_4Te_7$. The average laser fluence is 300 $\mu J/cm^2$ for the data sets presented here. (c) DFT-calculated slab bands for the structures indicated in (a) in the same row. The colored boxed areas in (c) and correspondingly colored arrows in (b) indicate regions of distinct dynamics labeled as α, β, and γ.

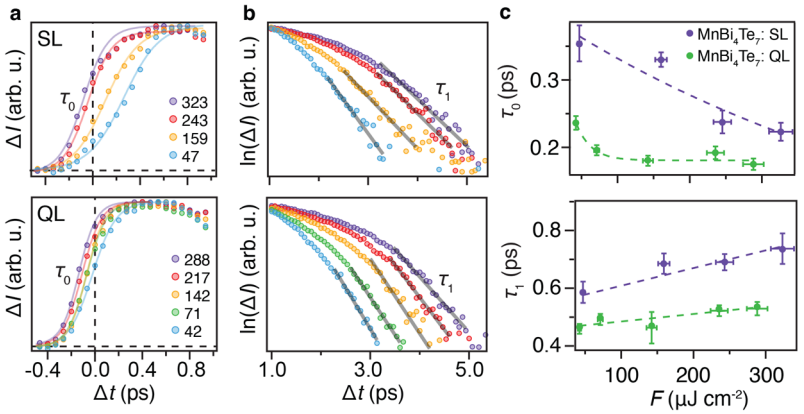

Figure 4. Charge transfer and phonon relaxation in $MnBi_4Te_7$. (a, b) (E, k)-integrated intensity difference from 0 to 70 meV above E_F and from -0.2 to 0.2 $Å^{-1}$ for SL and QL terminations of $MnBi_4Te_7$. Each data set was acquired with the fluence stated in (a) in units of $\mu J/cm^2$. In (a) we examine the rising edge of the signal (circles), representing the filling of unoccupied states above E_F, and fit a sigmoid function (curves) to extract the time scale τ_0 of the filling. In (b) we analyze the decay part of the signal on a logarithmic intensity scale and perform exponential fits (lines) to extract the phonon relaxation time scale τ_1. (c) Extracted time scales from (a) and (b) as a function of laser fluence. Dashed curves provide a guide to the eye.

layer-dependent contributions to the dynamics of the van der Waals-stacked $MnBi_2Te_4$ and Bi_2Te_3 layers of $MnBi_4Te_7$. In Figure 3a we inspect the transient occupation of both terminations via the intensity difference at $\Delta t = 40$ fs and compare it with $MnBi_2Te_4$ in a wider energy window in order to determine where the initially excited electrons are generated. The QL spectrum is characterized by a strong excitation signal 0.7 eV above E_F while only extremely faint intensity is present in this region at the SL termination, likely emerging from the next-nearest QL. These signals are consistent with spatially resolved pump−probe ARPES spectra obtained on the two terminations using a microfocused beam.[22] In analogy with Bi_2Te_3, the shallow excited band may be a surface resonance in the projected bulk band gap.[37] Indeed, our slab band structure calculations presented over a wider energy range in Figure 3c indicate that these are QL-derived bands that are absent in the $MnBi_2Te_4$ system, as seen via the region enclosed by a red box in Figure 3c.

Energy distribution curves (EDCs) extracted at Γ as a function of time delay, displayed in Figure 3b, reveal that the

band at 0.7 eV in the QL is instantaneously occupied followed by a rapid depopulation of excited electrons. Concomitantly, the electron and hole signals grow in the states closer to E_F in both the QL and the SL. The infrared pump pulse initially generates electron−hole pairs via direct transitions from the initially occupied states in both $MnBi_2Te_4$ and $MnBi_4Te_7$.[32,33] These include the states labeled α in Figure 3, as well as states at lower energy in the VB manifold. In $MnBi_2Te_4$, where the QL-derived state at 0.7 eV is absent, excitation proceeds via high-lying bulk states, followed by scattering directly to states close to E_F. See Figures S4 and S5 for further details on the bulk band structures and symmetries of the high-lying states. In $MnBi_4Te_7$, we propose that a fraction of excited carriers rapidly occupy the state at 0.7 eV (labeled γ) in the QLs of the van der Waals stack (on a faster time-scale than our experiment can resolve). Carriers are then extracted to the unoccupied states (labeled β) above E_F in both the QL and the SL via interband charge transfer with a time scale given by τ_0. A cascade of intraband scattering then results in excited carriers trickling down these states and finally recombining with holes via electron−phonon coupling on a time scale labeled as τ_1.

The optical tunability of inter- and intralayer charge transfer and phonon relaxation between the QL and the SL of $MnBi_4Te_7$ is demonstrated in Figure 4. We analyze the (E, k)-integrated intensity difference in the initially unoccupied states within 70 meV of E_F as a function of laser fluence and consider separately the rise part of the signal in Figure 4a and the decay part on a logarithmic intensity scale in Figure 4b. The initial increase of the signal in Figure 4a is highly fluence-dependent in the SL, exhibiting a significantly slower time scale with decreasing fluence, whereas the QL rise signal is faster and less sensitive to the fluence. In all cases, the rising part of the signal is well-described by a fit to a sigmoid function given by $(1 + \exp(2.35\Delta t/\tau_0))^{-1}$, providing an estimate of the charge transfer time, τ_0. After the initial increase in the intensity, the excited state population enters a plateau region. This occurs due to the competition between the charge being transferred from the γ-state in the QL into the β-states in both the SL and the QL and their subsequent recombination with holes. Finally, when the rate of refilling becomes slower than the electron−hole recombination processes, the transient occupation diminishes exponentially, as shown in Figure 4b. We quantify the time scale τ_1 of this process via the slope of a linear fit to the logarithm of the trace in Figure 4b.

The extracted fluence dependences of τ_0 and τ_1 are shown in Figure 4c. The growth rate of the population in the SL reaches a maximum of τ_0 = 0.35 ps at a low fluence of 47 μJ/cm^2, such that the population reaches its peak at around Δt = 0.80 ps. This is substantially delayed compared to the peak being reached around Δt = 0.40 ps for τ_0 = 0.22 ps at a high fluence of 323 μJ/cm^2. As we are considering the population in an energy range immediately above E_F, the rise time is strongly affected by interlayer charge transfer from the excited carriers in the γ-state in the QL. For low fluence, the intralayer filling of states from γ- to β-bands is more favorable than the interlayer charge transfer to the SL CB. Therefore, the filling rate of β-bands in the SL is slower for low excitation densities. For high excitation density, on the other hand, a large initial population is generated in the QL, thereby removing this bottleneck effect. For the QL termination, τ_0 exhibits a less dramatic fluence dependence and merely reflects the efficiency of intralayer interband scattering.

Finally, the decay time τ_1 provides information on electron−hole recombination. By comparison to the related systems Bi_2Se_3[33] and $Bi_2Se_xTe_{1-x}$ we infer that the relaxation is mediated by energy transfer to phonons. In particular, terahertz spectroscopy studies[38,39] show a similar fluence-dependent behavior of τ_1. The decay constant increases with applied fluence, indicating that the electron−phonon coupling becomes less efficient with a larger population of excited carriers. This trend can be explained by the increased screening of the electron−phonon interaction by the photoinduced charge carriers.[40] The relaxation dynamics extracted in Figure 4c are notably faster for QL than for SL, suggesting that intralayer phonons play a dominant role in the scattering processes. Such behavior is in line with a substantially weakened c-axis interlayer vibrational interaction in the heterostructure[41] in comparison to its nonmagnetic counterpart Bi_2Te_3.[42] We note, however, that we cannot distinguish between the involvement of in-plane and out-of-plane intralayer vibrational modes in the scattering process.

In conclusion, we have determined the ultrafast charge carrier dynamics of the intrinsic magnetic topological insulator van der Waals heterostructures $MnBi_2Te_4$ and $MnBi_4Te_7$. The out-of-equilibrium distribution of excited carriers exhibits distinct dynamics that is strongly affected by interlayer interactions between the Bi_2Te_3 quintuple layers and the $MnBi_2Te_4$ septuple layers. Infrared optical pumping leads to a transient population of carriers in the Bi_2Te_3 layers. These excited carriers are then extracted via interband and interlayer scattering into conduction band states around the Fermi energy within Bi_2Te_3 and in the adjacent $MnBi_2Te_4$ layers, respectively. In the regime of low laser fluence, the charge transfer processes into the $MnBi_2Te_4$ layers exhibit a bottleneck, potentially enabling optical control of the population of spin-polarized carriers in the magnetic layers of the van der Waals stack. Furthermore, as the subsequent electron−phonon-mediated relaxation is less efficient in the magnetic $MnBi_2Te_4$ compared to the nonmagnetic Bi_2Te_3 layers, it might be feasible to optically modify the magnetic properties of the heterostructure when designing spintronic and optoelectronic devices with layers of $MnBi_2Te_4$.

METHODS

Sample Growth. The $MnBi_2Te_4$ and $MnBi_4Te_7$ crystals were grown by the flux method. High purity Mn, Bi, and Te powders were sealed in quartz tubes with a Mn:Bi:Te ratio of 1:10:16. The tubes were heated to 900 °C and then cooled to 595/590 °C, respectively. The flux was removed by centrifugation after cooling.

Photoemission Experiments. The TR-ARPES measurements were performed at the T-ReX facility (Trieste, Italy). Pump and probe pulses were generated by a 250 kHz Ti:sapphire Coherent Reg A laser system, whose output was centered at an energy of 1.55 eV. The fourth harmonic (6.2 eV) of the fundamental beam was used as an s-polarized probe pulse. The remainder of the beam was used as a p-polarized pump with a tunable fluence in the range of 40−280 μJ/cm^2, arriving at the sample at a variable time delay, Δt, with respect to the probe. The experimental time, energy, and angular resolution were better than 200 fs, 50 meV and 0.2°, respectively. The samples were cleaved *in situ* at a base pressure of 2×10^{-10} mbar at room temperature and kept at a temperature of 100−110 K during the measurement.

Density Functional Theory Calculations. Band structures of $MnBi_2Te_4$ and $MnBi_4Te_7$ were calculated by DFT,[43,44] which was carried out by the Vienna ab initio simulation package (VASP)[45] based on the projector augmented wave (PAW) method.[46] The exchange-correlation functional was described by the generalized gradient approximation with the Perdew–Burke–Ernzerhof formalism (PBE)[47] with the on-site Coulomb interaction Hubbard U = 5 eV for electrons on d-orbitals of Mn atoms. The total energy convergence criteria were set to 1.0×10^{-6} eV including spin–orbit coupling (SOC). The plane-wave cutoff energy was set to 400 eV. We employed an $11 \times 11 \times 1$ Monkhorst–Pack grid to sample the whole Brillouin zone for both of the slab structures. Our slab band structures of $MnBi_2Te_4$ were obtained from slab calculations with the thickness of 6 van der Waals layers, while those of QL and SL terminations of $MnBi_4Te_7$ employed 5 and 7 van der Waals layers, respectively. The magnetic configurations were A-type AFM for both cases with 4.6 μB magnetic moments on the Mn atoms.

AUTHOR INFORMATION

Corresponding Author

Søren Ulstrup – *Department of Physics and Astronomy, Interdisciplinary Nanoscience Center, Aarhus University, 8000 Aarhus C, Denmark;* orcid.org/0000-0001-5922-4488; Email: ulstrup@phys.au.dk

Authors

Paulina Ewa Majchrzak – *Department of Physics and Astronomy, Interdisciplinary Nanoscience Center, Aarhus University, 8000 Aarhus C, Denmark;* orcid.org/0000-0002-5200-3866

Yuntian Liu – *Department of Physics and Shenzhen Institute for Quantum Science and Engineering (SIQSE), Southern University of Science and Technology, Shenzhen 518055, China*

Klara Volckaert – *Department of Physics and Astronomy, Interdisciplinary Nanoscience Center, Aarhus University, 8000 Aarhus C, Denmark*

Deepnarayan Biswas – *Department of Physics and Astronomy, Interdisciplinary Nanoscience Center, Aarhus University, 8000 Aarhus C, Denmark*

Chakradhar Sahoo – *Department of Physics and Astronomy, Interdisciplinary Nanoscience Center, Aarhus University, 8000 Aarhus C, Denmark*

Denny Puntel – *Dipartimento di Fisica, Università degli Studi di Trieste, 34127 Trieste, Italy*

Wibke Bronsch – *Elettra - Sincrotrone Trieste S.C.p.A., 34149 Basovizza, Italy;* orcid.org/0000-0002-6012-9290

Manuel Tuniz – *Dipartimento di Fisica, Università degli Studi di Trieste, 34127 Trieste, Italy*

Federico Cilento – *Elettra - Sincrotrone Trieste S.C.p.A., 34149 Basovizza, Italy*

Xing-Chen Pan – *Advanced Institute for Materials Research, Tohoku University, Sendai 980-8577, Japan*

Qihang Liu – *Department of Physics and Shenzhen Institute for Quantum Science and Engineering (SIQSE), Southern University of Science and Technology, Shenzhen 518055, China*

Yong P. Chen – *Department of Physics and Astronomy, Interdisciplinary Nanoscience Center, Aarhus University, 8000 Aarhus C, Denmark; Advanced Institute for Materials Research, Tohoku University, Sendai 980-8577, Japan; Department of Physics and Astronomy, School of Electrical and Computer Engineering, and Purdue Quantum Science and Engineering Institute, Purdue University, West Lafayette, Indiana 47907, United States*

Notes

The authors declare no competing financial interest.

ACKNOWLEDGMENTS

We gratefully acknowledge funding from VILLUM FONDEN through the Young Investigator Program (Grant. No. 15375), the Villum Investigator Program (Grant. No. 25931), the Centre of Excellence for Dirac Materials (Grant. No. 11744), and the Danish Council for Independent Research, Natural Sciences, under the Sapere Aude program (Grant No. DFF-9064-00057B). Work at the Advanced Institute for Materials Research has benefited from the support of WPI-AIMR, JSPS KAKENHI Basic Science A (18H03858), New Science (18H04473 and 20H04623), and Tohoku University FRiD program. C.S. acknowledges the Marie Sklodowska-Curie Postdoctoral Fellowship (Proposal Number 101059528). Work at SUSTech was supported by National Key R&D Program of China under Grant No. 2020YFA0308900 and the Center for Computational Science and Engineering of Southern University of Science and Technology.

REFERENCES

(1) Jin, C.; Ma, E. Y.; Karni, O.; Regan, E. C.; Wang, F.; Heinz, T. F. Ultrafast dynamics in van der Waals heterostructures. *Nat. Nanotechnol.* **2018**, *13*, 994–1003.

(2) Hong, X.; Kim, J.; Shi, S.-F.; Zhang, Y.; Jin, C.; Sun, Y.; Tongay, S.; Wu, J.; Zhang, Y.; Wang, F. Ultrafast charge transfer in atomically thin MoS2/WS2 heterostructures. *Nat. Nanotechnol.* **2014**, *9*, 682–686.

(3) Zheng, Q.; Saidi, W. A.; Xie, Y.; Lan, Z.; Prezhdo, O. V.; Petek, H.; Zhao, J. Phonon-Assisted Ultrafast Charge Transfer at van der Waals Heterostructure Interface. *Nano Lett.* **2017**, *17*, 6435–6442.

(4) Gong, Y.; Guo, J.; Li, J.; Zhu, K.; Liao, M.; Liu, X.; Zhang, Q.; Gu, L.; Tang, L.; Feng, X.; et al. Experimental realization of an intrinsic magnetic topological insulator. *Chin. Phys. Lett.* **2019**, *36*, 076801.

(5) Otrokov, M.; Rusinov, I. P.; Blanco-Rey, M.; Hoffmann, M.; Vyazovskaya, A. Y.; Eremeev, S.; Ernst, A.; Echenique, P. M.; Arnau, A.; Chulkov, E. V. Unique thickness-dependent properties of the van der Waals interlayer antiferromagnet MnBi 2 Te 4 films. *Physical review letters* **2019**, *122*, 107202.

(6) Zhang, D.; Shi, M.; Zhu, T.; Xing, D.; Zhang, H.; Wang, J. Topological axion states in the magnetic insulator MnBi 2 Te 4 with

the quantized magnetoelectric effect. *Physical review letters* **2019**, *122*, 206401.
(7) Li, J.; Li, Y.; Du, S.; Wang, Z.; Gu, B.-L.; Zhang, S.-C.; He, K.; Duan, W.; Xu, Y. Intrinsic magnetic topological insulators in van der Waals layered MnBi2Te4-family materials. *Science Advances* **2019**, *5*, No. eaaw5685.
(8) Otrokov, M. M.; Klimovskikh, I. I.; Bentmann, H.; Estyunin, D.; Zeugner, A.; Aliev, Z. S.; Gaß, S.; Wolter, A.; Koroleva, A.; Shikin, A. M.; et al. Prediction and observation of an antiferromagnetic topological insulator. *Nature* **2019**, *576*, 416−422.
(9) Deng, Y.; Yu, Y.; Shi, M. Z.; Guo, Z.; Xu, Z.; Wang, J.; Chen, X. H.; Zhang, Y. Quantum anomalous Hall effect in intrinsic magnetic topological insulator MnBi2Te4. *Science* **2020**, *367*, 895−900.
(10) Liu, C.; Wang, Y.; Li, H.; Wu, Y.; Li, Y.; Li, J.; He, K.; Xu, Y.; Zhang, J.; Wang, Y. Robust axion insulator and Chern insulator phases in a two-dimensional antiferromagnetic topological insulator. *Nat. Mater.* **2020**, *19*, 522−527.
(11) Zhao, Y.; Liu, Q. Routes to realize the axion-insulator phase in MnBi2Te4 (Bi2Te3) n family. *Appl. Phys. Lett.* **2021**, *119*, 060502.
(12) Gu, M.; Li, J.; Sun, H.; Zhao, Y.; Liu, C.; Liu, J.; Lu, H.; Liu, Q. Spectral signatures of the surface anomalous Hall effect in magnetic axion insulators. *Nat. Commun.* **2021**, *12*, 3524.
(13) Deng, H.; Chen, Z.; Wołoś, A.; Konczykowski, M.; Sobczak, K.; Sitnicka, J.; Fedorchenko, I. V.; Borysiuk, J.; Heider, T.; Pluciński, Ł.; Park, K.; Georgescu, A. B.; Cano, J.; Krusin-Elbaum, L. High-temperature quantum anomalous Hall regime in a MnBi2Te4/Bi2Te3 superlattice. *Nat. Phys.* **2021**, *17*, 36−42.
(14) Otrokov, M. M.; Menshchikova, T. V.; Vergniory, M. G.; Rusinov, I. P.; Yu Vyazovskaya, A.; Koroteev, Y. M.; Bihlmayer, G.; Ernst, A.; Echenique, P. M.; Arnau, A.; Chulkov, E. V. Highly-ordered wide bandgap materials for quantized anomalous Hall and magnetoelectric effects. *2D Materials* **2017**, *4*, 025082.
(15) Sun, H.; Xia, B.; Chen, Z.; Zhang, Y.; Liu, P.; Yao, Q.; Tang, H.; Zhao, Y.; Xu, H.; Liu, Q. Rational design principles of the quantum anomalous Hall effect in superlatticelike magnetic topological insulators. *Physical review letters* **2019**, *123*, 096401.
(16) Wu, J.; Liu, F.; Sasase, M.; Ienaga, K.; Obata, Y.; Yukawa, R.; Horiba, K.; Kumigashira, H.; Okuma, S.; Inoshita, T.; et al. Natural van der Waals heterostructural single crystals with both magnetic and topological properties. *Science advances* **2019**, *5*, No. eaax9989.
(17) Xu, L.; et al. Persistent surface states with diminishing gap in MnBi2Te4/Bi2Te3 superlattice antiferromagnetic topological insulator. *Science Bulletin* **2020**, *65*, 2086−2093.
(18) Hu, Y.; Xu, L.; Shi, M.; Luo, A.; Peng, S.; Wang, Z. Y.; Ying, J. J.; Wu, T.; Liu, Z. K.; Zhang, C. F.; Chen, Y. L.; Xu, G.; Chen, X.-H.; He, J.-F. Universal gapless Dirac cone and tunable topological states in $(MnBi_2Te_4)_m(Bi_2Te_3)_n$ heterostructures. *Phys. Rev. B* **2020**, *101*, 161113.
(19) Wu, X.; Li, J.; Ma, X.-M.; Zhang, Y.; Liu, Y.; Zhou, C.-S.; Shao, J.; Wang, Q.; Hao, Y.-J.; Feng, Y.; et al. Distinct topological surface states on the two terminations of MnBi 4 Te 7. *Physical Review X* **2020**, *10*, 031013.
(20) Hu, C.; Gordon, K. N.; Liu, P.; Liu, J.; Zhou, X.; Hao, P.; Narayan, D.; Emmanouilidou, E.; Sun, H.; Liu, Y.; et al. A van der Waals antiferromagnetic topological insulator with weak interlayer magnetic coupling. *Nat. Commun.* **2020**, *11*, 97.
(21) Lu, R.; Sun, H.; Kumar, S.; Wang, Y.; Gu, M.; Zeng, M.; Hao, Y.-J.; Li, J.; Shao, J.; Ma, X.-M.; et al. Half-magnetic topological insulator with magnetization-induced Dirac gap at a selected surface. *Physical Review X* **2021**, *11*, 011039.
(22) Yan, C.; Green, E.; Fukumori, R.; Protic, N.; Lee, S. H.; Fernandez-Mulligan, S.; Raja, R.; Erdakos, R.; Mao, Z.; Yang, S. An integrated quantum material testbed with multi-resolution photoemission spectroscopy. *Rev. Sci. Instrum.* **2021**, *92*, 113907.
(23) Nevola, D.; Li, H. X.; Yan, J.-Q.; Moore, R. G.; Lee, H.-N.; Miao, H.; Johnson, P. D. Coexistence of Surface Ferromagnetism and a Gapless Topological State in $MnBi_2Te_4$. *Phys. Rev. Lett.* **2020**, *125*, 117205.
(24) Zhong, H.; Bao, C.; Wang, H.; Li, J.; Yin, Z.; Xu, Y.; Duan, W.; Xia, T.-L.; Zhou, S. Light-Tunable Surface State and Hybridization Gap in Magnetic Topological Insulator MnBi8Te13. *Nano Lett.* **2021**, *21*, 6080−6086.
(25) Li, H.; et al. Dirac Surface States in Intrinsic Magnetic Topological Insulators $EuSn_2As_2$ and $MnBi_{2n}Te_{3n+1}$. *Phys. Rev. X* **2019**, *9*, 041039.
(26) Estyunin, D. A.; Klimovskikh, I. I.; Shikin, A. M.; Schwier, E. F.; Otrokov, M. M.; Kimura, A.; Kumar, S.; Filnov, S. O.; Aliev, Z. S.; Babanly, M. B.; Chulkov, E. V. Signatures of temperature driven antiferromagnetic transition in the electronic structure of topological insulator MnBi2Te4. *APL Materials* **2020**, *8*, 021105.
(27) Yan, C.; Fernandez-Mulligan, S.; Mei, R.; Lee, S. H.; Protic, N.; Fukumori, R.; Yan, B.; Liu, C.; Mao, Z.; Yang, S. Origins of electronic bands in the antiferromagnetic topological insulator $MnBi_2Te_4$. *Phys. Rev. B* **2021**, *104*, L041102.
(28) Zeugner, A.; Nietschke, F.; Wolter, A. U. B.; Gaß, S.; Vidal, R. C.; Peixoto, T. R. F.; Pohl, D.; Damm, C.; Lubk, A.; Hentrich, R.; et al. Chemical Aspects of the Candidate Antiferromagnetic Topological Insulator MnBi2Te4. *Chem. Mater.* **2019**, *31*, 2795−2806.
(29) Hao, Y.-J.; et al. Gapless Surface Dirac Cone in Antiferromagnetic Topological Insulator $MnBi_2Te_4$. *Phys. Rev. X* **2019**, *9*, 041038.
(30) Li, H.; et al. Dirac Surface States in Intrinsic Magnetic Topological Insulators $EuSn_2As_2$ and $MnBi_{2n}Te_{3n+1}$. *Phys. Rev. X* **2019**, *9*, 041039.
(31) Chen, Y. J.; et al. Topological Electronic Structure and Its Temperature Evolution in Antiferromagnetic Topological Insulator $MnBi_2Te_4$. *Phys. Rev. X* **2019**, *9*, 041040.
(32) Hajlaoui, M.; Papalazarou, E.; Mauchain, J.; Lantz, G.; Moisan, N.; Boschetto, D.; Jiang, Z.; Miotkowski, I.; Chen, Y. P.; Taleb-Ibrahimi, A.; Perfetti, L.; Marsi, M. Ultrafast Surface Carrier Dynamics in the Topological Insulator Bi2Te3. *Nano Lett.* **2012**, *12*, 3532−3536.
(33) Sobota, J. A.; Yang, S.; Analytis, J. G.; Chen, Y. L.; Fisher, I. R.; Kirchmann, P. S.; Shen, Z.-X. Ultrafast Optical Excitation of a Persistent Surface-State Population in the Topological Insulator Bi_2Se_3. *Phys. Rev. Lett.* **2012**, *108*, 117403.
(34) Crepaldi, A.; Ressel, B.; Cilento, F.; Zacchigna, M.; Grazioli, C.; Berger, H.; Bugnon, P.; Kern, K.; Grioni, M.; Parmigiani, F. Ultrafast photodoping and effective Fermi−Dirac distribution of the Dirac particles in Bi_2Se_3. *Phys. Rev. B* **2012**, *86*, 205133.
(35) Wu, X.; et al. Distinct Topological Surface States on the Two Terminations of $MnBi_4Te_7$. *Phys. Rev. X* **2020**, *10*, 031013.
(36) Vidal, R. C.; et al. Orbital Complexity in Intrinsic Magnetic Topological Insulators $MnBi_4Te_7$ and $MnBi_6Te_{10}$. *Phys. Rev. Lett.* **2021**, *126*, 176403.
(37) Sánchez-Barriga, J.; Battiato, M.; Krivenkov, M.; Golias, E.; Varykhalov, A.; Romualdi, A.; Yashina, L. V.; Minár, J.; Kornilov, O.; Ebert, H.; Held, K.; Braun, J. Subpicosecond spin dynamics of excited states in the topological insulator Bi_2Te_3. *Phys. Rev. B* **2017**, *95*, 125405.
(38) Li, G.; Zhou, W.; Zhang, W.; Ma, G.; Cui, H.; Gao, Y.; Huang, Z.; Chu, J. Pump fluence dependence of ultrafast carrier dynamics in InSb measured by optical pump-terahertz probe spectroscopy. *Appl. Opt.* **2018**, *57*, 9729−9734.
(39) Reinhoffer, C.; Mukai, Y.; Germanskiy, S.; Bliesener, A.; Lippertz, G.; Uday, A.; Taskin, A. A.; Ando, Y.; Wang, Z.; van Loosdrecht, P. H. M. Relaxation dynamics of the optically driven nonequilibrium states in the electron- and hole-doped topological-insulator materials $(Bi_{1-x}Sb_x)_2Te_3$. *Phys. Rev. Materials* **2020**, *4*, 124201.
(40) Heid, R.; Sklyadneva, I. Y.; Chulkov, E. V. Electron-phonon coupling in topological surface states: The role of polar optical modes. *Sci. Rep.* **2017**, *7*, 1095.
(41) Cho, Y.; Kang, J. H.; Liang, L.; Taylor, M.; Kong, X.; Ghosh, S.; Kargar, F.; Hu, C.; Balandin, A. A.; Puretzky, A. A.; Ni, N.; Wong, C. W. Phonon modes and Raman signatures of $MnBi_{2n}Te_{3n+1}$(n = 1, 2, 3,

4) magnetic topological heterostructures. *Phys. Rev. Research* **2022**, *4*, 013108.
(42) Liang, L.; Zhang, J.; Sumpter, B. G.; Tan, Q.-H.; Tan, P.-H.; Meunier, V. Low-Frequency Shear and Layer-Breathing Modes in Raman Scattering of Two-Dimensional Materials. *ACS Nano* **2017**, *11*, 11777−11802.
(43) Hohenberg, P.; Kohn, W. Inhomogeneous Electron Gas. *Phys. Rev.* **1964**, *136*, B864−B871.
(44) Kohn, W.; Sham, L. J. Self-Consistent Equations Including Exchange and Correlation Effects. *Phys. Rev.* **1965**, *140*, A1133−A1138.
(45) Kresse, G.; Furthmüller, J. Efficient iterative schemes for ab initio total-energy calculations using a plane-wave basis set. *Phys. Rev. B* **1996**, *54*, 11169−11186.
(46) Kresse, G.; Joubert, D. From ultrasoft pseudopotentials to the projector augmented-wave method. *Phys. Rev. B* **1999**, *59*, 1758−1775.
(47) Perdew, J. P.; Burke, K.; Ernzerhof, M. Generalized Gradient Approximation Made Simple. *Phys. Rev. Lett.* **1996**, *77*, 3865−3868.